10. G. F. Bignami, P. A. Caraveo, R. C. Lamb, T. H. Markert, J. A. Paul, *Astrophys. J.* **247**, L85 (1981).
11. C. Motch, F. Haberl, K. Dennerl, M. Pakull, E. Janot-Pacheco, *Astron. Astrophys.* **323**, 853 (1997).
12. K. Bernlöhr et al., *Astropart. Phys.* **20**, 111 (2003).
13. J. A. Hinton, *N. Astron. Rev.* **48**, 331 (2004).
14. S. Funk et al., *Astropart. Phys.* **22**, 285 (2004).
15. F. Aharonian et al., *Science* **307**, 1938 (2005).
16. F. Aharonian et al., *Astropart. Phys.* **22**, 109 (2004).
17. M. de Naurois et al., in *28th International Cosmic Ray Conference*, T. Kajita et al., Eds. (Universal Academy Press, Tokyo, 2003), p. 2907.
18. F. Piron et al., *Astron. Astrophys.* **374**, 895 (2001).
19. M. Ribó et al., *Astron. Astrophys.* **384**, 954 (2002).
20. J. J. Condon et al., *Astron. J.* **115**, 1693 (1998).
21. A. Martocchia, C. Motch, I. Negueruela, *Astron. Astrophys.* **430**, 245 (2005).
22. V. Bosch-Ramon, J. M. Paredes, *Astron. Astrophys.* **417**, 1075 (2004).
23. R. J. Gould, G. P. Schréder, *Phys. Rev.* **155**, 1408 (1967).
24. S. Corbel et al., *Science* **298**, 196 (2002).
25. L. Maraschi, A. Treves, *Mon. Not. R. Astron. Soc.* **194**, 1P (1981).
26. M. Beilicke, M. Ouchrif, G. Rowell, S. Schlenker, *IAU Circ.* **8300**, 2 (2004).
27. N. J. Tasker, J. J. Condon, A. E. Wright, M. R. Griffith, *Astron. J.* **107**, 2115 (1994).
28. M. Ribó, P. Reig, J. Martí, J. M. Paredes, *Astron. Astrophys.* **347**, 518 (1999).
29. J. Martí, J. M. Paredes, M. Ribó, *Astron. Astrophys.* **338**, L71 (1998).
30. J. S. Clark et al., *Astron. Astrophys.* **376**, 476 (2001).
31. The support of the Namibian authorities and of the University of Namibia in facilitating the construction and operation of HESS is gratefully acknowledged, as is the support of the German Ministry for Education and Research (BMBF), the Max Planck Society, the French Ministry for Research, the CNRS-IN2P3 and the Astroparticle Interdisciplinary Programme of the CNRS, the UK Particle Physics and Astronomy Research Council (PPARC), the IPNP of Charles University, the South African Department of Science and Technology and National Research Foundation, and the University of Namibia. We appreciate the excellent work of the technical support staff in Berlin, Durham, Hamburg, Heidelberg, Palaiseau, Paris, Saclay, and Namibia in the construction and operation of the equipment. L.C., C.M., M.O., and M.T. are also affiliated with the European Associated Laboratory for Gamma-Ray Astronomy, jointly supported by CNRS and the Max Planck Society.

Spectroscopy Using Quantum Logic

P. O. Schmidt,*† T. Rosenband, C. Langer, W. M. Itano,
J. C. Bergquist, D. J. Wineland

We present a general technique for precision spectroscopy of atoms that lack suitable transitions for efficient laser cooling, internal state preparation, and detection. In our implementation with trapped atomic ions, an auxiliary "logic" ion provides sympathetic laser cooling, state initialization, and detection for a simultaneously trapped "spectroscopy" ion. Detection is achieved by applying a mapping operation to each ion, which results in a coherent transfer of the spectroscopy ion's internal state onto the logic ion, where it is then measured with high efficiency. Experimental realization, by using ^{9}Be$^+$ as the logic ion and ^{27}Al$^+$ as the spectroscopy ion, indicates the feasibility of applying this technique to make accurate optical clocks based on single ions.

The continued development of atomic-state manipulation techniques has led to improvements in physical measurements and devices. A good example of this improvement is in the area of atomic spectroscopy, where increases in resolution and accuracy to levels better than 1 part in 10^{15} (*1, 2*) have been achieved with atomic clocks. This, in turn, has improved tests of fundamental theories (*3*). To achieve these levels of performance in spectroscopy, four key requirements are as follows: (i) selection of an atom with a good reference or "spectroscopy" transition, which is suitably narrow and relatively immune to environmental perturbations; (ii) cooling to minimize velocity-induced frequency shifts; (iii) reliable initial state preparation; and (iv) efficient state detection.

Previously, to satisfy these requirements, an atom was chosen that simultaneously had a good spectroscopy transition and other, more strongly allowed transitions to accomplish requirements (ii) to (iv) (*1, 2*). Here we describe how two different atomic species can share these requirements, so that one species need only have a good spectroscopy transition, and the other species can fulfill the other three requirements, as outlined in (*4*). We demonstrate this technique experimentally with trapped atomic ions.

To describe the transfer protocol, we consider two atomic ions of different species located on the weak axis of a three-dimensional trap. We designate one of the ions as the logic ion and the other as the spectroscopy ion, and we treat the internal states of the ions as two-level systems with eigenstates labeled $|\downarrow\rangle$ and $|\uparrow\rangle$. The Coulomb interaction of the ions couples their motion, which is best described in a normal-mode basis (*5–7*). All normal modes are assumed to be initially cooled to near their ground states by Doppler laser cooling on the logic ion, which sympathetically cools the spectroscopy ion (*8*).

One of the ions' normal modes (which has harmonic oscillator states labeled $|n\rangle_m$, where n denotes the nth level of the mode m) is chosen as the transfer mode on which the state mapping is implemented. This mode is cooled to its ground state (*7*). Figure 1A shows both ions and the transfer mode in their ground states, described by the wave function $\psi_0 = |\downarrow\rangle_S|\downarrow\rangle_L|0\rangle_m$, where the indices S and L denote

the spectroscopy and logic ion, respectively. We excite the spectroscopy transition by applying coherent radiation tuned near the spectroscopy ion's transition resonance (Fig. 1B), leading to

$$\Psi_0 \rightarrow \Psi_1 = (\alpha|\downarrow\rangle_S + \beta|\uparrow\rangle_S)|\downarrow\rangle_L|0\rangle_m$$

$$= (\alpha|\downarrow\rangle_S|0\rangle_m + \beta|\uparrow\rangle_S|0\rangle_m)|\downarrow\rangle_L \quad (1)$$

where $|\alpha|^2 + |\beta|^2 = 1$. We now drive a red sideband (RSB) π pulse (*5, 9*) on the spectroscopy ion (Fig. 1C) so that

$$\Psi_1 \rightarrow \Psi_2 = (\alpha|\downarrow\rangle_S|0\rangle_m + \beta|\downarrow\rangle_S|1\rangle_m)|\downarrow\rangle_L$$

$$= |\downarrow\rangle_S|\downarrow\rangle_L(\alpha|0\rangle_m + \beta|1\rangle_m) \quad (2)$$

thereby mapping the spectroscopy ion's internal state to the transfer mode, which is shared by both ions. During the mapping process, a transient entanglement is created between the internal state of the ^{27}Al$^+$ ion and the motional state. The $|\downarrow\rangle_S|0\rangle_m$ component of the wave function is unaffected by this operation, because the state $|\uparrow\rangle_S|-1\rangle_m$ does not exist (*5, 9*); this is the key element of quantum logic used here (*10, 11*). We apply a final RSB π pulse on the logic ion (Fig. 1D), which yields

$$\Psi_2 \rightarrow \Psi_{\text{final}} = |\downarrow\rangle_S(\alpha|\downarrow\rangle_L + \beta|\uparrow\rangle_L)|0\rangle_m \quad (3)$$

and thereby completes the mapping of the spectroscopy ion's state onto the logic ion.

The logic ion is next measured (not shown in Fig. 1), projecting its state to $|\downarrow\rangle_L$ or $|\uparrow\rangle_L$, which can be efficiently distinguished. By repeating this experiment many times, we can determine the probabilities $|\alpha|^2$ and $|\beta|^2$ as functions of the spectroscopy probe frequency and thereby determine the spectroscopy ion's transition frequency.

We implemented the technique with a single ^{9}Be$^+$ logic ion (*5, 11*) and a single ^{27}Al$^+$ spectroscopy ion (Fig. 2) simultaneously trapped in a linear Paul trap similar to that de-

Time and Frequency Division, National Institute of Standards and Technology, 325 Broadway, Boulder, CO 80305, USA.

*Present address: Institut für Experimentalphysik, Universität Innsbruck, Technikerstrasse 25, A-6020 Innsbruck, Austria.
†To whom correspondence should be addressed. E-mail: piet.schmidt@uibk.ac.at

scribed in (12). Our choice for $^{27}Al^+$ was motivated by its potential as a high-accuracy optical clock based on the $^1S_0 \leftrightarrow {}^3P_0$ reference transition, which has a Q factor of $Q \equiv f/\Delta f \approx 2 \times 10^{17}$, where f is the frequency of the transition and Δf is its width (13). Although it was previously considered (14, 15), $^{27}Al^+$ has not yet been used as an optical frequency standard because it lacks an accessible cooling transition.

As a demonstration of the technique, we probed the magnetic substates of the $|^1S_0, F = 5/2\rangle \rightarrow |^3P_1, F' = 7/2\rangle$ transitions, where F and F' are the total angular momentum quantum numbers of the ground and excited state, respectively, in $^{27}Al^+$ [wavelength $\lambda \approx 267$ nm, natural linewidth $\Gamma/2\pi \approx 520$ Hz (16)]. We drove these transitions with a frequency-doubled dye laser that had been stabilized to an isolated high-finesse cavity (17), yielding a spectral linewidth of less than 6 Hz. Two separately switchable probe laser beams, incident at 45° with respect to the weak trap axis, were π- and $\hat{\sigma}^{+/-}$-polarized, respectively.

The $^9Be^+$ system, with $|\downarrow\rangle_L \equiv |^2S_{1/2}, F = 2, m_F = -2\rangle$ and $|\uparrow\rangle_L \equiv |^2S_{1/2}, F' = 1, m_{F'} = -1\rangle$, where m_F is the magnetic quantum number of the total angular momentum F, has been described in detail (7, 11). The trap provides single $^9Be^+$ trap frequencies of $\omega_z \approx 2\pi \times 3.8$ MHz along the weak axis (z axis) and $\omega_x \approx$ $2\pi \times 13.8$ MHz and $\omega_y \approx 2\pi \times 14.9$ MHz orthogonal to the weak trap axis. We performed Doppler cooling with a $\hat{\sigma}^-$-polarized laser beam tuned to the $^9Be^+ |\downarrow\rangle_L \rightarrow |^2P_{3/2}, F'' = 3, m_{F''} = -3\rangle$ transition. Counting fluorescence photons on this cycling transition also allowed us to determine the $^9Be^+$ ion's final measured state, because an ion in $|\downarrow\rangle_L$ fluoresces strongly, whereas an ion in $|\uparrow\rangle_L$ fluoresces negligibly for this laser frequency (11, 14). State rotations and resolved-sideband cooling on $^9Be^+$ were performed by means of two-photon stimulated Raman pulses on $|\downarrow\rangle_L|n\rangle_m \leftrightarrow |\uparrow\rangle_L|n'\rangle_m$ transitions (5, 11).

Raman sideband cooling of the two axial modes, optical pumping of $^9Be^+$ (7, 11), and state preparation of the spectroscopy ion (see below) initialize the ion pair to the state $|\downarrow\rangle_S|\downarrow\rangle_L|0\rangle_m$, which is the starting point for the spectroscopy protocol described above. State transfer was carried out using the in-phase weak-axis mode (7).

Figure 3A shows experimental data for single–laser pulse (Rabi) spectroscopy of the $^{27}Al^+$ $|^1S_0, F = 5/2, m_F = 5/2\rangle = |\downarrow\rangle_S \rightarrow |^3P_1, F' = 7/2, m_{F'} = 7/2\rangle = |\uparrow\rangle_S$ transition. We applied interrogation pulses of constant intensity and duration, corresponding to approximate π pulses on this transition when the laser beam was tuned to resonance. An experimental se-

quence took ~ 1 ms and was repeated 700 times per data point. The observed linewidth of the transition is Fourier-transform–limited with a fitted full width at half maximum linewidth of 63 kHz for an excitation pulse duration of $t_\pi = 12.6$ μs. The observed contrast of 93% (normalized to the contrast of a $^9Be^+$ sideband transition) was limited by the spontaneous decay of the $^{27}Al^+$ $^3P_1$ state during the protocol and by a shot-to-shot variation of the Rabi frequency caused by fluctuations of phonon number in the Doppler-cooled radial modes (Debye-Waller reduction factors) (18, 19).

Figure 3B shows internal state oscillations on the aluminum ion obtained by varying the interrogation duration t_i (on-resonance Rabi flopping) (5). The observed coherence time of 118 μs was limited by the ≈ 305-μs lifetime of the $^3P_1$ excited state, Rabi frequency fluctuations caused by the radial motion Debye-Waller factors, and magnetic field fluctuations.

We verified the coherence of the transfer process by performing a Ramsey experiment in which the first (optical) $\pi/2$ pulse created a superposition state in the aluminum ion. This coherence was then mapped to the beryllium
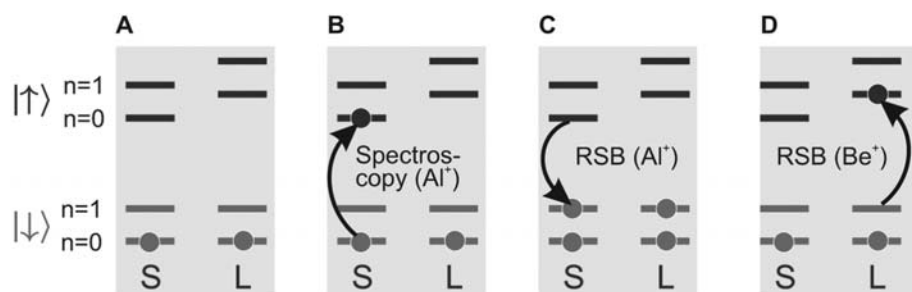
Fig. 1. Spectroscopy and transfer scheme for spectroscopy (S) and logic (L) ions sharing a common normal mode of motion, the transfer mode, with excitation n. (Only the ground and first excited states of the transfer mode are shown.) (**A**) Initialization to the ground internal and transfer-mode states. (**B**) Interrogation of the spectroscopy transition. (**C**) Coherent transfer of the internal superposition state of the spectroscopy ion into a motional superposition state by use of an RSB π pulse on the spectroscopy ion. (**D**) Coherent transfer of the motional superposition state into an internal superposition state of the logic ion by use of an RSB π pulse on the logic ion.
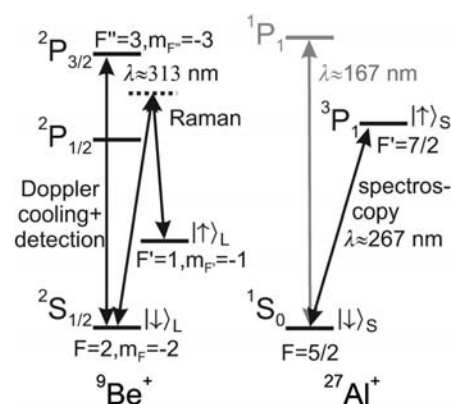
Fig. 2. Partial $^9Be^+$ and $^{27}Al^+$ energy level diagrams (not to scale). Shown are the relevant transitions for Doppler and Raman cooling on the $^9Be^+$ ion, the spectroscopy transition, and the difficult-to-reach Doppler cooling transition at 167 nm on the $^{27}Al^+$ ion.
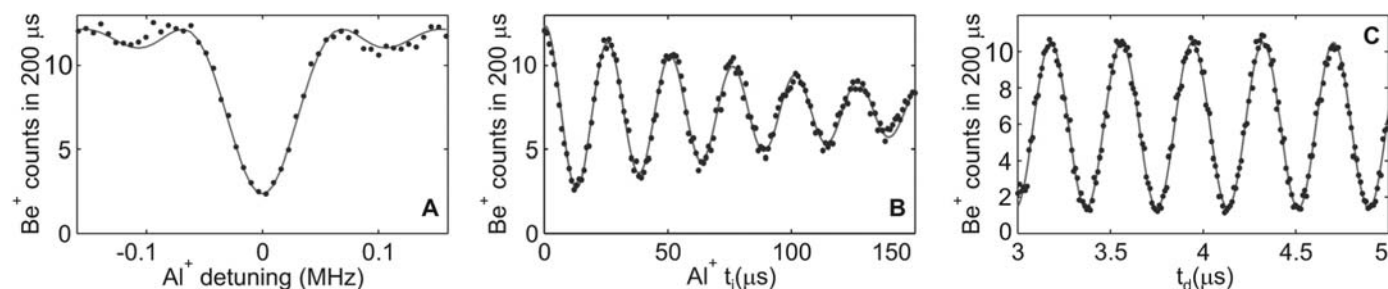
Fig. 3. (**A**) Rabi spectroscopy of the $|^1S_0, F = 5/2, m_F = 5/2\rangle \rightarrow |^3P_1, F' = 7/2, m_{F'} = 7/2\rangle$ transition in $^{27}Al^+$, showing a frequency scan across the resonance. The data (black circles) are fit by the theoretically expected probability $P_{\downarrow,S}$ of finding $^{27}Al^+$ in the ground state after applying the probe pulse. (**B**) Rabi flopping at the center frequency of the transition in (A). The data are fit by an exponentially damped sinusoidal function. (**C**) Two-ion Ramsey time scan. The data are fit by a sinusoidal function.

ion, where it was probed with a second (Raman transition corresponding to a radio frequency) $\pi/2$ pulse applied to the beryllium ion. Between the two Ramsey pulses, we mapped the aluminum ion's internal state onto the transfer mode, waited a duration t_d, and then mapped the transfer mode state onto the beryllium ion. Figure 3C shows a plot of the detected population $P_{\downarrow,L}$ of the beryllium ion versus t_d. This signal oscillates with a frequency corresponding to the transfer mode frequency. The optical phases of the logic ion and spectroscopy ion laser beams do not need to be stabilized from experiment to experiment, because the phase between the states $|\downarrow\rangle_L$ and $|\uparrow\rangle_L$ after the last Ramsey pulse depends on the phase differences between the two pulses applied to each ion, both of which were held constant over all experiments (20).

The spectroscopy protocol does not depend on phase coherence between the laser pulses, because we measure only the spectroscopy ion's state probabilities $|\alpha|^2$ and $|\beta|^2$. However, the coherence of the process can be useful; for example, the Ramsey experiment provides a sensitive way to measure and correct for drifts in the mode frequency. (For this purpose, it is, in practice, easier to perform both Ramsey and mapping pulses on the $^9Be^+$ ion.)

In spectroscopy experiments, initial state preparation is often accomplished with optical pumping on a strongly allowed transition. Because such a transition may not be accessi-ble in the spectroscopy atom, we can again rely on quantum logic methods for state preparation. The process for preparing the $^{27}Al^+$ $|\downarrow\rangle_S \equiv |^1S_0, F = 5/2, m_F = +5/2\rangle$ state is outlined in Fig. 4A. If we assume that the transfer mode is initialized in its ground state, each stage of the preparation process is composed of three steps: (i) a $\hat{\pi}$-polarized, m_F-preserving ($m_{F'} = m_F$) π pulse that does not change the motional state ("carrier" transition); (ii) a $\hat{\sigma}^-$-polarized, m_F-changing ($m_F = m_{F'} + 1$) RSB π pulse; and (iii) a laser cooling stage (on the $^9Be^+$ ion) that puts the transfer mode back into its ground state. The cooling stage incorporates spontaneous emission, which is required in normal optical pumping and makes the RSB π pulse irreversible, hence insuring irreversibility of the overall process. We can "sweep" the population to the desired state $m_F = +5/2$ by sequentially applying these three steps to the $m_F = -5/2, -3/2, \ldots, +3/2$ ground states (in Fig. 4A, only the transfer from the $m_F = +1/2$ and $+3/2$ states is shown). By adapting this procedure, we can prepare any of the $^{27}Al^+$ ground states. In Fig. 4B, we show $\Delta m_F = 0$ spectroscopy on all Zeeman states of the $^{27}Al^+$ $|^1S_0, F = 5/2\rangle \rightarrow |^3P_1, F' = 7/2\rangle$ transition in a magnetic field of 3 mT (chosen to spectrally resolve all transitions) by using this state preparation technique.

We demonstrated in a separate experiment that the effect of optical pumping of the $^{27}Al^+$ during deterministic preparation is negligible. For this purpose, we replaced the RSB pulse in all preparation stages with a wait time of the same duration, thereby allowing for $^{27}Al^+$ $^3P_1 \rightarrow$ $^1S_0$ radiative decay during the remaining time (<1.5 ms) of the stage. Figure 4C shows the contrast of the $^{27}Al^+$ $m_F = +5/2 \rightarrow m_{F'} = +5/2$ transition, normalized to the $m_F = +5/2 \rightarrow m_{F'} = +7/2$ transition, as a function of the number of preparation repetitions for both cases. The deterministic preparation achieves the maximum contrast after a single preparation sequence, whereas we observed only a slow increase in contrast for optical pumping (21). This result also demonstrates that initial state preparation of spectroscopy ions can be achieved without depending on spontaneous emission from their excited state, which is particularly important for ions with a long-lived excited state, as in the case of the $^{27}Al^+$ $^1S_0 \leftrightarrow {}^3P_0$ clock transition.

We have demonstrated spectroscopy using quantum logic, a technique for precision atomic spectroscopy that removes the requirements of efficient cooling, state preparation, and state detection from the species upon which the spectroscopy is performed. Although we have implemented this technique with atomic ions, it may also be applicable to other systems for which quantum logic techniques are being developed, including neutral atoms (22, 23) and perhaps molecules with simple internal state structure. This technique offers a way to investigate new atomic ion species and their potential for providing reference transitions for high-accuracy optical clocks, such as the $^1S_0 \leftrightarrow {}^3P_0$ transitions in $^{27}Al^+$ and $^{10}B^+$ (4, 15) or optical transitions in He^+ (24, 25). Because coherence of the transfer process is not required for spectroscopy, it should be possible to detect transitions in the spectroscopy ion by detecting the recoil upon absorption (24). On the other hand, the coherence in the transfer process could be beneficial in quantum information experiments, where the information could be distributed between different species, thereby simplifying the laser beam addressing of adjacent quantum bits.
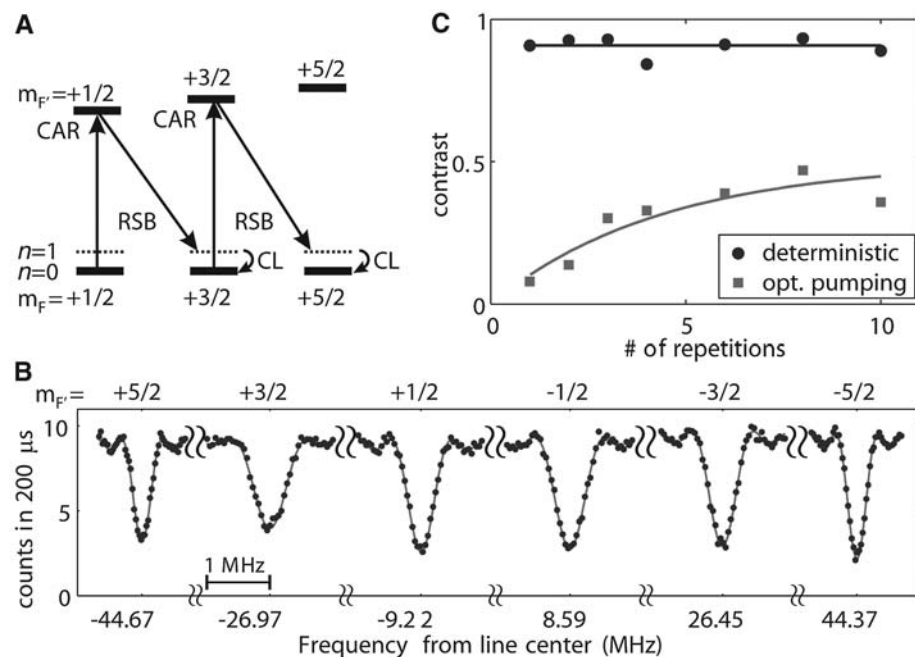
Fig. 4. Deterministic state preparation of the spectroscopy ion. (**A**) The last steps of the deterministic preparation of the $m_F = +5/2$ ground state consist of $\hat{\pi}$-polarized carrier (CAR) π pulses followed by $\hat{\sigma}^-$-polarized RSB π pulses on $^{27}Al^+$ and ground state cooling on $^9Be^+$ (CL), to ensure irreversibility of the sequence. (**B**) Carrier Rabi spectroscopy of all $\hat{\pi}$-polarized transitions in $^{27}Al^+$ using deterministic preparation. (**C**) Normalized contrast of the $m_F = +5/2 \rightarrow +5/2$ $\hat{\pi}$-polarized transition versus number of preparation repetitions for optical pumping and the deterministic preparation. The lines are guides to the eye.

References and Notes
1. P. Gill, Ed., *Proceedings of the 6th Symposium on Frequency Standards and Metrology* (World Scientific, Singapore, 2002).
2. S. A. Diddams, J. C. Bergquist, S. R. Jefferts, C. W. Oates, *Science* **306**, 1318 (2004).
3. S. G. Karshenboim, E. Peik, Eds., *Astrophysics, Clocks and Fundamental Constants,* Lecture Notes in Physics 648 (Springer, Berlin, Heidelberg, 2004).
4. D. J. Wineland, J. C. Bergquist, J. J. Bollinger, R. E. Drullinger, W. M. Itano, in *Proceedings of the 6th Symposium on Frequency Standards and Metrology,* P. Gill, Ed. (World Scientific, Singapore, 2002), pp. 361–368.
5. D. J. Wineland *et al., J. Res. Nat. Inst. Stand. Technol.* **103**, 259 (1998).
6. G. Morigi, H. Walther, *Eur. Phys. J. D* **13**, 261 (2000).
7. M. D. Barrett *et al., Phys. Rev. A.* **68**, 042302 (2003).
8. D. J. Larson, J. C. Bergquist, J. J. Bollinger, W. M. Itano, D. J. Wineland, *Phys. Rev. Lett.* **57**, 70 (1986).
9. D. M. Meekhof, C. Monroe, W. M. Itano, B. E. King, D. J. Wineland, *Phys. Rev. Lett.* **76**, 1796 (1996).

10. J. I. Cirac, P. Zoller, *Phys. Rev. Lett.* **74**, 4091 (1995).
11. C. Monroe, D. M. Meekhof, B. E. King, W. M. Itano, D. J. Wineland, *Phys. Rev. Lett.* **75**, 4714 (1995).
12. M. A. Rowe *et al.*, *Quant. Inform. Comp.* **2**, 257 (2002).
13. W. M. Itano, unpublished calculation.
14. H. G. Dehmelt, *IEEE Trans. Instrum. Meas.* **IM-31**, 83 (1982).
15. N. Yu, H. Dehmelt, W. Nagourney, *Proc. Natl. Acad. Sci. U.S.A.* **89**, 7289 (1992).
16. E. Träbert, A. Wolf, J. Linkemann, X. Tordoir, *J. Phys. B At. Mol. Opt. Phys.* **32**, 537 (1999).
17. B. Young, F. Cruz, W. Itano, J. Bergquist, *Phys. Rev. Lett.* **82**, 3799 (1999).
18. D. J. Wineland, W. M. Itano, *Phys. Rev. A.* **20**, 1521 (1979).
19. For long interrogation times, sideband cooling on the logic ion can be applied during and/or after interrogation of the spectroscopy transition (before the first

coherent transfer step, Fig. 1C), thus eliminating a degradation of linewidth and contrast caused by transfer mode heating during interrogation.
20. Methods are available as supporting materials on *Science* Online.
21. We did not prepare the ion in any particular state before each experiment. Rather, competition between state preparation and off-resonant depumping determined the distribution of polarizations before the next repetition of the experiment.
22. K. Eckert *et al.*, *Phys. Rev. A.* **66**, 042317 (2002).
23. E. Charron, E. Tiesinga, F. Mies, C. Williams, *Phys. Rev. Lett.* **88**, 077901 (2002).
24. B. Roth, U. Fröhlich, S. Schiller, *Phys. Rev. Lett.* **94**, 053001 (2005).
25. M. Herrmann *et al.*, in preparation.
26. We thank S. Diddams, J. Koelemeij, and J. Ye for stim-

Electron Localization Determines Defect Formation on Ceria Substrates

Friedrich Esch,[1]*** Stefano Fabris,**[2] **Ling Zhou,**[3]
Tiziano Montini,[4,5] **Cristina Africh,**[1,5,6] **Paolo Fornasiero,**[4,5]
Giovanni Comelli,[1,5,6] **Renzo Rosei**[1,5,6]

The high performance of ceria (CeO_2) as an oxygen buffer and active support for noble metals in catalysis relies on an efficient supply of lattice oxygen at reaction sites governed by oxygen vacancy formation. We used high-resolution scanning tunneling microscopy and density functional calculations to unravel the local structure of surface and subsurface oxygen vacancies on the (111) surface. Electrons left behind by released oxygen localize on cerium ions. Clusters of more than two vacancies exclusively expose these reduced cerium ions, primarily by including subsurface vacancies, which therefore play a crucial role in the process of vacancy cluster formation. These results have implications for our understanding of oxidation processes on reducible rare-earth oxides.

Materials based on ceria (CeO_2) are used in the production and purification of hydrogen, the purification of exhaust gases in three-way automotive catalytic converters, and other catalytic applications (*1–4*). In all such applications, highly mobile lattice oxygen is involved in oxidation processes. Over a wide range of working temperatures (from room temperature to 1000°C), ceria plays two key roles: (i) releasing and storing oxygen, and (ii) promoting noble-metal activity and dispersion (*3, 5*).

Both phenomena are controlled by the type, size, and distribution of oxygen vacancies as the most relevant surface defects. In the case of transition-metal oxide surfaces, a thorough characterization of these vacancies has led to greater understanding of the fundamental features of the reactivity (*6–9*) and to the design of efficient supported catalysts (*10*). This knowledge has been lacking for the rare-earth oxides, but their chemistry is likely different because excess electrons left behind by the removal of neutral oxygen localize on empty f states. In ceria, this results in the valence change $Ce^{4+} \rightarrow Ce^{3+}$ of two cations per vacancy and in an extraordinary efficiency for reversible oxygen release (*3, 11, 12*). Reduction drastically modifies the reactivity of ceria substrates (*13, 14*).

Oxygen vacancies are also crucial for the binding of catalytically active species to ceria (*3*). The high activity of Au/ceria catalysts in the water-gas shift reaction has recently been traced back to highly dispersed, ionic Au species that form only in the presence of defects (*15, 16*).

The control of the density and the nature of oxygen vacancies could provide a means for tailoring the reactivity of ceria-based catalysts. However, despite extensive spectroscopic, microscopic, and diffraction studies, a detailed atomic-level insight into the local defect struc-ture, defect mobility, and valence of the cerium ions is still missing (*3, 11, 12, 14, 17–21*).

Ceria crystallizes in a cubic fluorite structure and exposes the thermodynamically most stable (111) surface (*3*). This surface is the oxygen termination of stoichiometric O-Ce-O trilayers stacked along the [111] direction and also represents the major fraction of the active surface in catalytic nanocrystallites (*12*).

We report high-resolution scanning tunneling microscopy (STM) results on CeO_2(111), which we interpret in light of density functional theory (DFT) calculations. The single-crystal sample was cleaned by repeated cycles of sputtering and annealing to 900°C. Annealing at this temperature leads to oxygen release and is therefore a means to control the degree of surface reduction of the sample. Although ceria is an insulator (band gap 6 eV), its reduction and the elevated temperatures used in this study (300° to 400°C) enhance the electron conductivity (*3*). Furthermore, the elevated temperatures considerably suppress the adsorption of species from the ultrahigh vacuum chamber background (10^{-10} mbar, mainly H_2, H_2O, and CO) that would interfere with the microscope tip. In this way, atomic resolution could be obtained with STM in large-scale images (Fig. 1). The DFT calculations are based on an advanced implementation (*22–24*) that captures full electron localization on Ce 4f states in a manner not directly accessible to standard DFT calculations (*25*). Filled-state images are shown to map the positions of the outermost oxygen atoms. Their local relaxation around the defects discriminates between different defect geometries.

Various defects had already been observed in earlier STM and atomic force microscopy studies of ceria at lower temperatures (*17–21*), but on a small scale and with limited resolution that precluded a discussion of their relative distribution. Moreover, Namai *et al.* reported defect mobility even at room temperature (*20, 21*). These results are in contrast to our observations: None of the defects shown in Fig. 1 is mobile on a time scale of minutes. Direct diffusion of vacancies (i.e., hopping of lattice oxygen) on this surface requires temperatures

[1]Laboratorio Nazionale Tecnologie Avanzate e Nanoscienza (TASC)–Istituto Nazionale per la Fisica della Materia (INFM), 34012 Trieste, Italy. [2]Scuola Internazionale Superiore di Studi Avanzati (SISSA) and INFM Democritos National Simulation Center, 34014 Trieste, Italy. [3]Institute of Physical Chemistry and Electrochemistry, University of Hannover, D-30167 Hannover, Germany. [4]Chemistry Department and Consorzio Interuniversitario Nazionale per la Scienza e Tecnologia dei Materiali (INSTM), [5]Center of Excellence for Nanostructured Materials (CENMAT), [6]Physics Department, University of Trieste, 34127 Trieste, Italy.

*To whom correspondence should be addressed. E-mail: friedrich.esch@elettra.trieste.it